TECHNICAL ARTICLE

Constitutive and Artificial Neural Network Modeling to Predict Hot Deformation Behavior of CoFeMnNiTi Eutectic High-Entropy Alloy

Reliance Jain, Priyanka Umre, Rama Krushna Sabat, Vinod Kumar, and Sumanta Samal

In the present work, the Arrhenius-type constitutive equation and artificial neural network (ANN) model have been used to predict the hot deformation behavior of CoFeMnNiTi eutectic high-entropy alloy in the temperature range 1073-1273 K and strain rate range 0.001-1 s^{-1}. The performance of both models is assessed by using the coefficient of correlation (R) and average absolute relative error (AARE). The ANN model with $R = 0.9997$ and AARE = 1.52 % better predicts flow behavior than the Arrhenius type model with $R = 0.9769$ and AARE = 11.5 %. The rate of softening and mean free path value are also evaluated at different thermomechanical conditions to understand the deformation mechanism. The compressive flow behavior of EHEA also studied and understood the softening and globularization phenomenon during deformation and proposed the deformation mechanism.

1. Introduction

In last few years, there have been surge in research activities in the exciting field of high-entropy alloys (HEAs) domain to design and develop novel materials with unique microstructure. It is reported that HEAs comprise four or more major elements with a concentration between 5 and 35 atomic % (Ref 1, 2). Eutectic high-entropy alloys (EHEAs) are composed of solid solution phase and intermetallics and having good strength and ductility (Ref 3). In the stress–strain plot, drop in the flow stress after reaching the peak stress is recognized to either the mechanism of DRX (dynamic recrystallization) or globularization of phase. DRX phenomena are related to the hot working temperature, strain rate, and the initial grain size of the alloys. In a stress–strain plot, the formation of single or multiple peaks may also define the DRX mechanism. Generally, low strain rate and high temperature during the deformation in HEAs favor the DRX (Ref 4). Stepanov et al. (Ref 5) described the hot working at different temperatures and strain rates and also DRX mechanism for CoCrFeMnNi HEA (during uniaxial compression to a height reduction of 75%, corresponding to a true strain of ≈1.4). They observed the discontinuous type DRX is main mechanism associated with microstructure evolution during all

deformation temperatures (873-1373 K). At temperatures above 1073 K, bulgings were observed in initial grain boundaries, and nucleation of new grains along the initial grain boundaries taken place, while below 1073 K, the shear band deformation was observed in the deformed sample. In the past, numerous constitutive models have been established to characterize alloy flow behavior at high temperatures (Ref 6). The various models have been used to understand the hot working of materials under different processing conditions, such as Johnson-cook (J-C) (Ref 7) model, Zerilli–Armstrong (Z-A) (Ref 8) model, and hyperbolic sinusoidal Arrhenius relation proposed for a broad range of stress (Ref 9). Also, several reformations to this established model have been recommended to improve its results. As reported in the literature, the J-C model is not suitable for predicting softening behavior during hot deformation. Also, the model does not accurately track flow stress at a higher strain rate and lower temperature due to the lack of information on various deformation phenomena. (Ref 10). Motlagh et al. (Ref 10) reported the prediction of flow behavior at different hot working conditions (temperature range of 1173-1323 K and at strain rates of 0.001-1 s^{-1}) for 1.4542 stainless steel by different models. In the literature, it is found that the performance of the Arrhenius model is better than J-C and Z-A model. In J-C and Z-A models, the effects on flow stress by strain, temperature, and strain rate are separated, so these models accuracy cannot satisfactorily predict the flow stress. Patnamsetty et al. (Ref 11) deliberated the flow behavior at thermomechanical conditions for CoCrFeMnNi HEA using the Arrhenius relation and predicted the flow curve over a wide temperature (1023-1423 K) and strain rates (0.001-10 s^{-1}) ranges. The conventional models have specific limitations to predict the flow behavior, such that J-C model has not considered the thermal softening effect for flow stress prediction. While physics-based Z-A model considers the strain hardening, thermal softening, and other physical effects for flow stress prediction, it uses some parameters which are estimated using precision equipment. The Arrhenius relation

Reliance Jain, Priyanka Umre, Vinod Kumar, and Sumanta Samal, Department of Metallurgy Engineering and Materials Science, Indian Institute of Technology Indore, Indore, India; Rama Krushna Sabat, School of Minerals, Metallurgical and Materials Engineering, Indian Institute of Technology Bhubaneswar, Bhubaneswar 752050, India. Contact e-mail: sumanta@iiti.ac.in.

Table 1 Performance of the model

Model performance	R	AARE (%)
Sine hyperbolic Arrhenius model	0.9769	11.50
ANN model 1		
$\quad X_{\text{nor.}} = 0.1 + 0.8 \times \frac{(X - X_{\min})}{(X_{\max} - X_{\min})}$	0.9897	3.45
$\quad$ Normalization of all input parameters (σ, T, and $\dot{\varepsilon}$)		
ANN model 2		
$\quad \dot{\varepsilon}_{\text{nor.}} = 0.1 + 0.8 \times \frac{(\log \dot{\varepsilon} - \log \dot{\varepsilon}_{\min})}{(\log \dot{\varepsilon}_{\max} - \log \dot{\varepsilon}_{\min})}$	0.9997	1.52
$\quad$ Normalization of Strain rate ($\dot{\varepsilon}$), while Stress (σ) and Temperature (T) normalized by as per the ANN model 1		

estimates the activation energy of the material during the deformation and gives the information about the deformation mechanism which is correlated with the microstructural evolution, mainly dislocation movement, dynamic recovery (DRV), DRX and grain boundary movement.

An ANN is a digital form of the human brain that abstracts the data by learning from the available data and observes the patterns in the form of input/output without any prior assumption. ANN approach offers unprecedented opportunities to solve complex problems, i.e., nonlinear systems and uneven data prediction (Ref 12). Sabokpa et al. (Ref 13) predicted the flow stress using the ANN approach at temperature range 523-673 K and strain rate 0.0001 to 0.01 s^{-1} for AZ81 magnesium alloy. Singh et al. (Ref 14) predicted the flow behavior during hot deformation of phosphorus steel using the ANN method. Therefore, ANN has recently emerged as a promising modeling approach to predict different parameters in materials engineering. However, only a few studies predict the flow curve of EHEAs at different processing conditions during deformation using the strain compensated constitution equation. Reliance et al. (Ref 15) reported the microhardness prediction using ANN approach for different HEAs and FeCoNiCrMnVAlNb EHEAs with respect to their compositions. Reliance et al. (Ref 6) predicted flow behavior at different hot deformation conditions using ANN approach for CoCrFeNiZr containing HEA. From the literature, it was observed that there is a limited study to predict flow behavior during hot deformation of EHEAs using the ANN approach.

The current study established an Arrhenius relation and multilayer perceptron ANN model with Levenberg–Marquardt (L-M) algorithm to predict flow stress. Finally, the proposed model's predictability is evaluated based on the coefficient of correlation (R) and average absolute relative error (AARE). Furthermore, to understand the mechanism of softening and DRX during the hot deformation, the deformation mechanism is proposed.

2. Materials and Methods

For assessing the flow stress by an Arrhenius relation and ANN model, experimental flow stress data of hot compression tested samples of studied EHEAs with different hot working conditions (temperature range 1073-1273 K and strain rate range 0.001-1 s^{-1}) were collected from our previous study of hot workability of $Co_{25}Fe_{25}Mn_5Ni_{25}Ti_{20}$ EHEA (Ref 16). For the flow curve prediction in the present study, MATLAB 9.6

(R2019b) version has been used. Before performing the training, the data are first normalized in a range of 0-1 for accurate predictions. But the deviation in strain rate is found to be large, and after normalization, the amount of strain rate is minimal, which is not appropriately learned by ANN in the present study. Further, the logarithm equation is used to normalize the strain rate. The normalization procedure of data for training purposes is given in Table 1 (Ref 17).

The ANN model is established to examine the flow curve by using the neural network using the L-M training algorithm. The input of that model is the strain, temperature, and strain rate, and the outcome is flow stress. A total of 624 data points were employed for the ANN model.

3. Result and Discussion

3.1 Flow Curve Prediction Using Constitution Model for $Co_{25}Fe_{25}Mn_5Ni_{25}Ti_{20}$ EHEA

Many researchers currently use the constitutive relation based on the Arrhenius relation to estimate the flow stress during hot working (Ref 18), but accuracy usually is limited. Further, the improvement in the model is by considering the Zener–Holloman parameter (Z) (Ref 19). The respective governing equation is given as:

$$Z = A_0 \times \left[\sinh(\alpha \sigma_f) \right]^n = \dot{\varepsilon} \times \exp\left(\frac{Q_h}{RT} \right) \qquad \text{(Eq 1)}$$

$$\dot{\varepsilon} = A_0 \times \left[\sinh(\alpha \sigma_f) \right]^n \times \exp\left(-\frac{Q_h}{RT} \right) \qquad \text{(Eq 2)}$$

where $\dot{\varepsilon}$ represents the strain rate (s^{-1}), Q_h represents the activation energy (J/mol) during hot working processing, R represents the universal gas constant 8.314 J/(mol·K), T is the temperature in K, σ_f represents the flow stress (MPa), and A_0, α, and n are the material constants. Constant α is estimated by the ratio of β/N, where β and N are the slopes of the lnσ vs. ln $\dot{\varepsilon}$ and σ versus ln $\dot{\varepsilon}$ plot with a linear fit. The value of n is the slope of ln $\dot{\varepsilon}$ versus ln[sinh($\alpha\sigma$)] plot with a linear fit. Q_h is expressed in equation 5. In equation 3, the value of s is the slope of the linear fit of 10,000/T versus ln[sinh($\alpha\sigma$)]. Figure 1(a)-(d) shows the plots for calculation of constant β, N, n, and s, respectively. Constant A_0 can be estimated by taking the logarithm of Eq 1 can be given in Eq 4 (Ref 19).

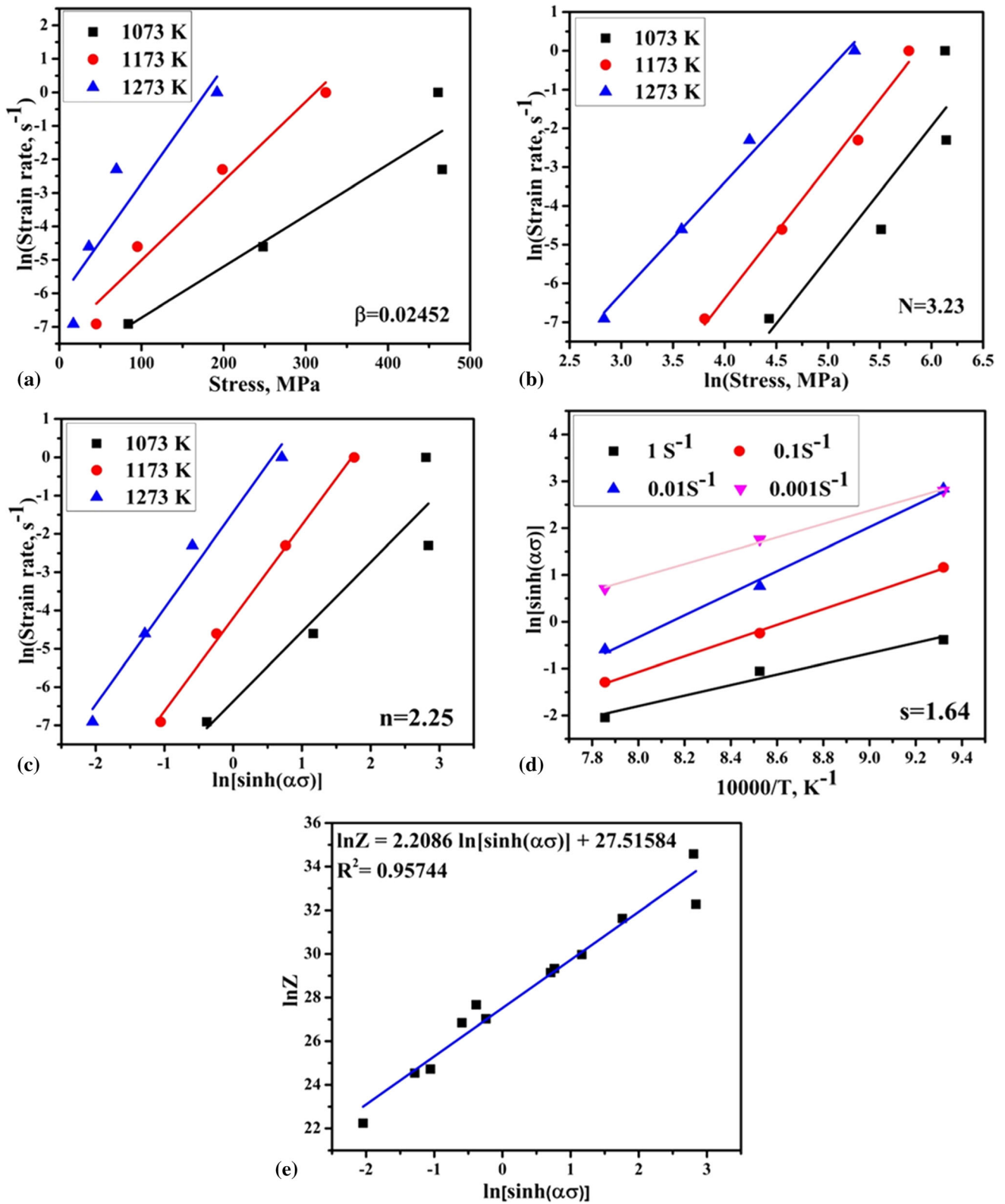$$Q_h = 10,000 \times R \times (n)_T \times (s)_{\dot{\varepsilon}} \qquad \text{(Eq 3)}$$

Fig. 1 Plots for different material constants (a) *β*, (b) *N*, (c) *n*, (d) *s*, and (e) *lnA₀*
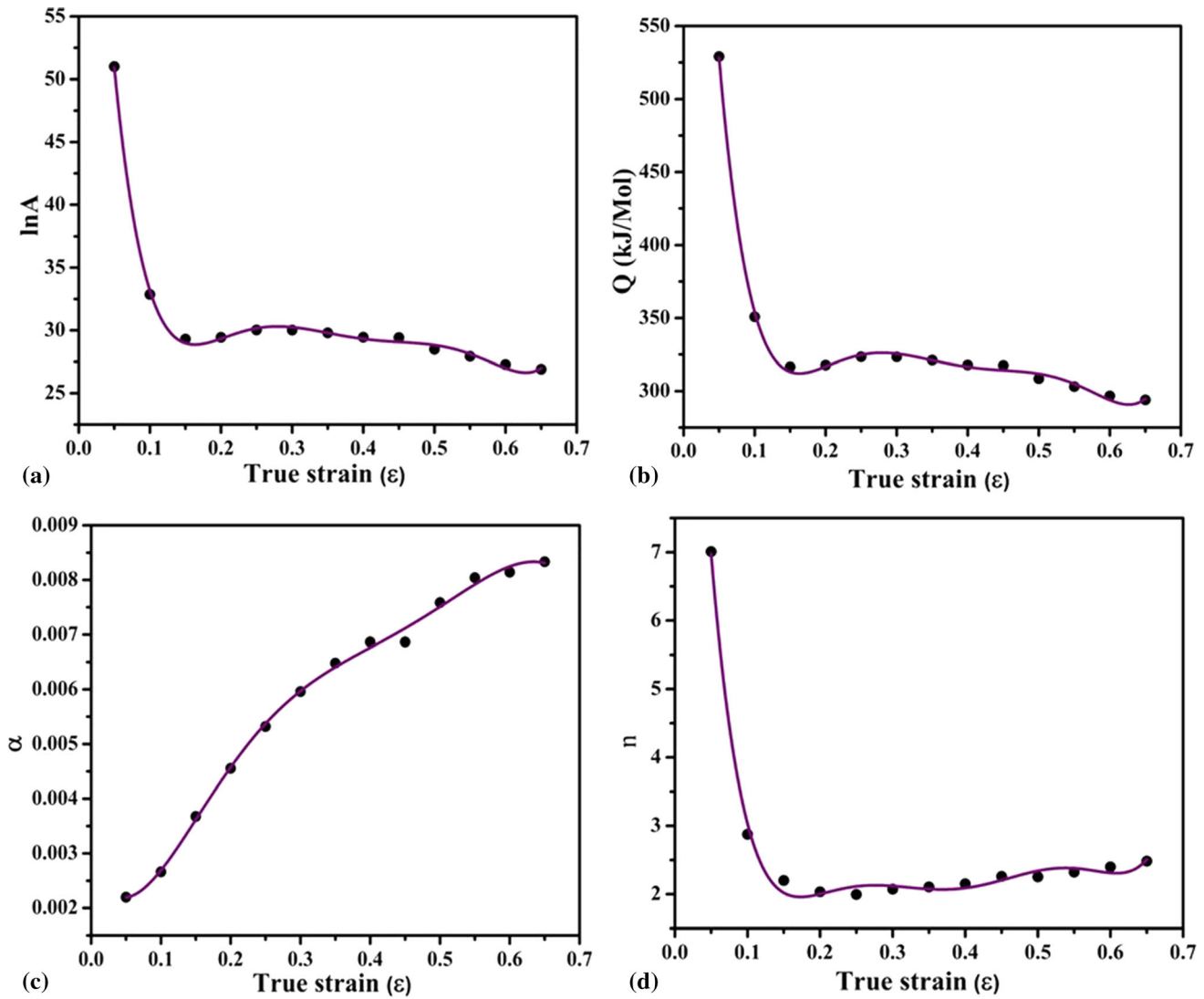
Fig. 2 Variation on material constant (α, Q, n, and A_0) with strain

$$\ln Z = \ln A_0 + n \ln\left[\sinh\left(\alpha\sigma_f\right)\right] \tag{Eq 4}$$

The intercept of the linear relation between the $\ln[\sinh(\alpha\sigma_f)]$ versus $\ln Z$ provides the value of $\ln A_0$(as given in Fig. 1(e)). Lastly, the relationship of σ_f, Z, A_0, and α can be written as:

$$\sigma_f = \frac{1}{\alpha} \times \ln\left\{ \left(\frac{Z}{A_0}\right)^{\frac{1}{n}} + \left[\left(\frac{Z}{A_0}\right)^{\frac{2}{n}} + 1\right]^{\frac{1}{2}} \right\} \tag{Eq 5}$$

The n is calculated as an average of the slopes of $\left\{(\partial \ln \dot{\varepsilon}) / \partial \ln\left[\sinh\left(\alpha\sigma_f\right)\right]\right\}$ at different temperatures because the n is dependent on strain rate and temperature. Q_h is calculated by putting a value of R, n, and s in Eq 3 at strain 0.5 (at strain 0.5 value of $\beta = 0.024$, $\alpha = 0.0076$, $N = 3.23$, $n = 2.25$, and s = 1.64), which is approximately 308468 J/mol. The parameters Z, $\dot{\varepsilon}$ and σ at strain 0.5 can be expressed as the following equation:

$$Z_{0.5} = \dot{\varepsilon} \times \exp\left(\frac{308468}{RT}\right) \tag{Eq 6}$$

$$\dot{\varepsilon} = 8.91 \times 10^{11} \times \left[\sinh\left(0.0076\sigma_{f0.5}\right)\right]^{2.25} \times \dot{\varepsilon} \times \exp\left(\frac{308468}{RT}\right) \tag{Eq 7}$$

$$\sigma_{f0.5} = \frac{1}{0.0076}$$
$$\times \ln\left\{ \left(\frac{Z_{0.5}}{8.11 \times 10^{11}}\right)^{\frac{1}{2.25}} + \left[\left(\frac{Z_{0.5}}{8.11 \times 10^{11}}\right)^{\frac{2}{2.25}} + 1\right]^{\frac{1}{2}} \right\} \tag{Eq 8}$$

Figure 2 shows the variation of strain on constant (α, Q, n, and A_0). For calculating the flow stress at different strains, the
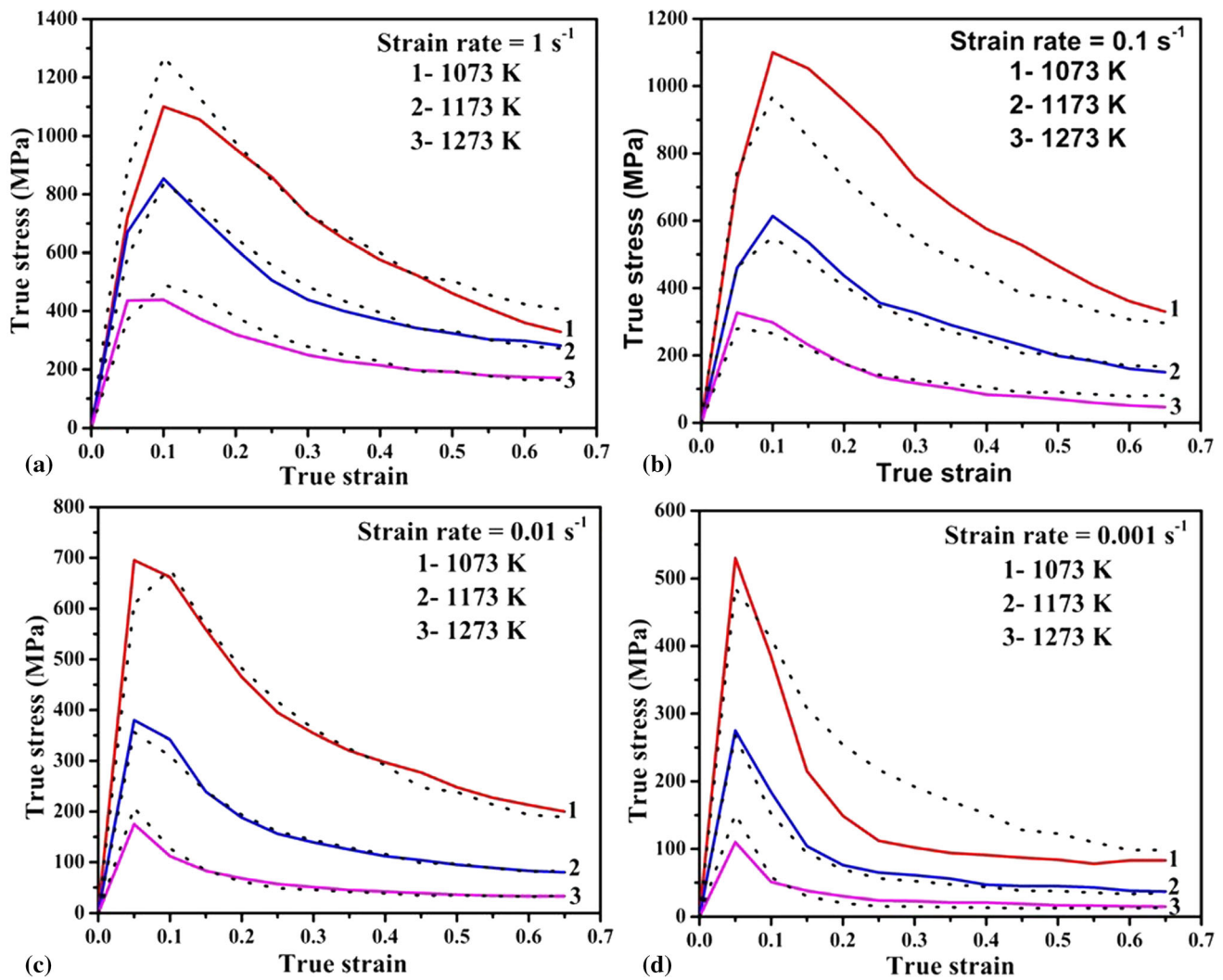
Fig. 3 Representation of predicted flow stress (dotted line) and actual flow stress (solid line) using the Arrhenius model

material constant (α, Q, n, and A_0) is calculated by the polynomial fitting and is fitted by sixth order, which is found to be a good correlation with strain and can be expressed as:

$$\ln A_0 = -1398.168\varepsilon + 10936.386\varepsilon^2 - 42533.268\varepsilon^3$$
$$+ 87846.688\varepsilon^4 - 92303.215\varepsilon^5 + 38800.137\varepsilon^6$$
$$+ 98.276$$

$$(Eq\ 9)$$

$$Q = -13773.473\varepsilon + 107945.454\varepsilon^2 - 42.663.603\varepsilon^3$$
$$+ 870539.300\varepsilon^4 - 916452.012\varepsilon^5 + 385959.408\varepsilon^6$$
$$+ 994.608$$

$$(Eq\ 10)$$

$$\alpha = -0.03011\varepsilon + 0.42851\varepsilon^2 - 1.6888\varepsilon^3 + 3.0726\varepsilon^4$$
$$- 2.5599\varepsilon^5 + 0.74712\varepsilon^6 + 0.00282$$

$$(Eq\ 11)$$

$$n = -305.584\varepsilon + 2385.786\varepsilon^2 - 9362.457\varepsilon^3 + 19592.326\varepsilon^4$$
$$- 20831.632\varepsilon^5 + 8823.861\varepsilon^6 + 17.339$$

$$(Eq\ 12)$$

3.2 Flow Behavior Prediction Using the ANN Model

The 3-15-1 network system of ANN model predicts flow stress with optimum accuracy after several trains, where the 15 shows neurons in the hidden layer. The network with 15 neurons in the hidden layer gives the best possible result (mean square error and coefficient of correlation). For ANN modeling, 156 datasets are used; among these, 110 datasets (70 %) are used in training, 23 datasets (15%) are used for validation, and 23 datasets (15%) are used in testing.

3.3 Performance of the Models

Finally, Fig. 3 and 4 shows the predicted flow stress (dotted line) with actual flow stress (solid line) at different hot working conditions using the Arrhenius relation and ANN model 2.
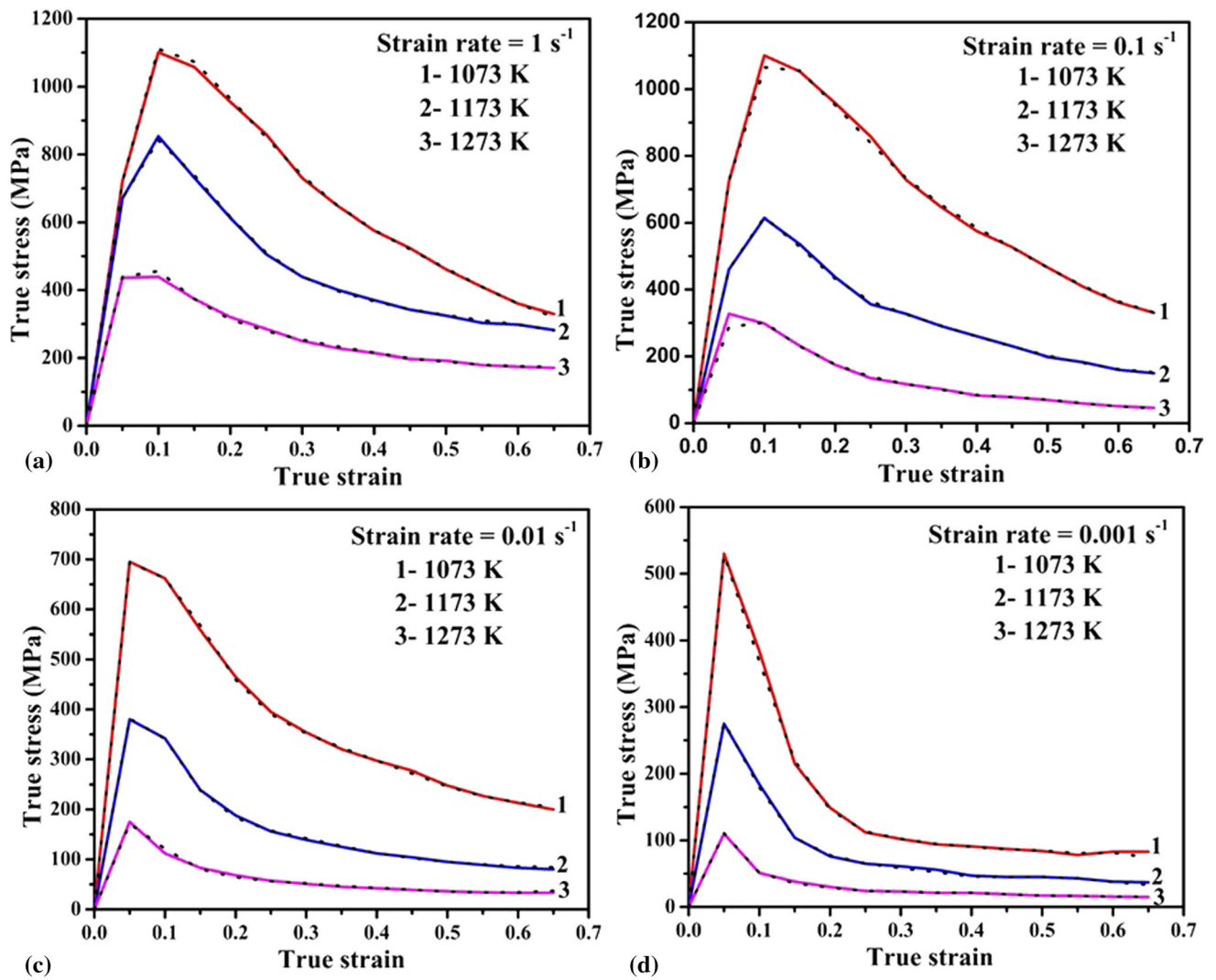
Fig. 4 Representation of predicted flow stress (dotted line) and experimental flow stress (solid line) using the ANN model 2
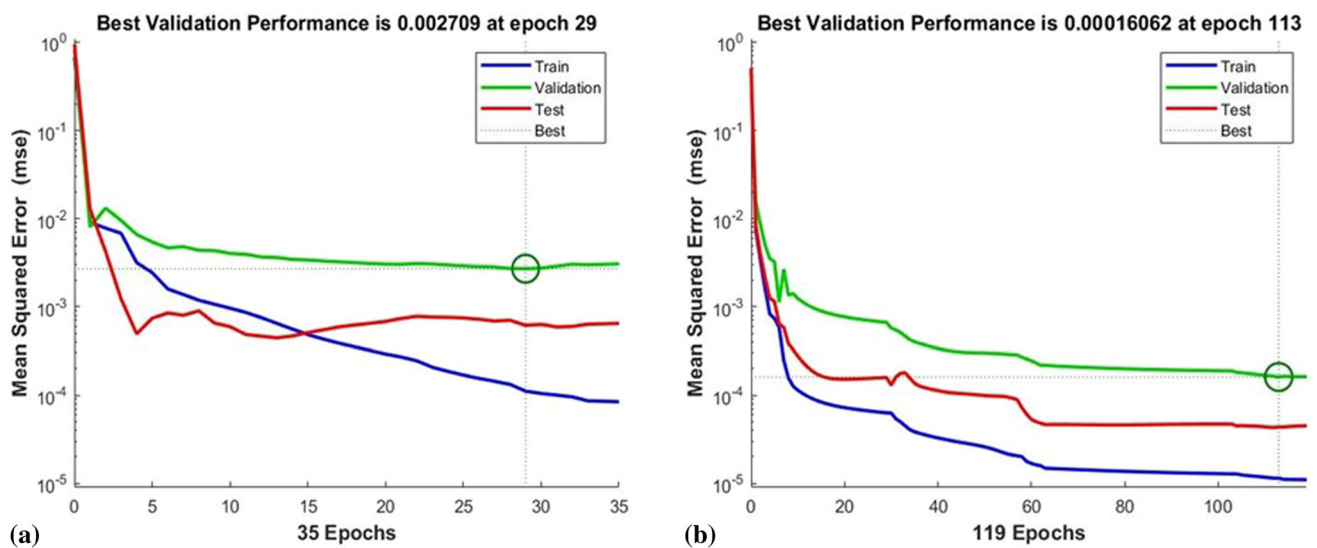

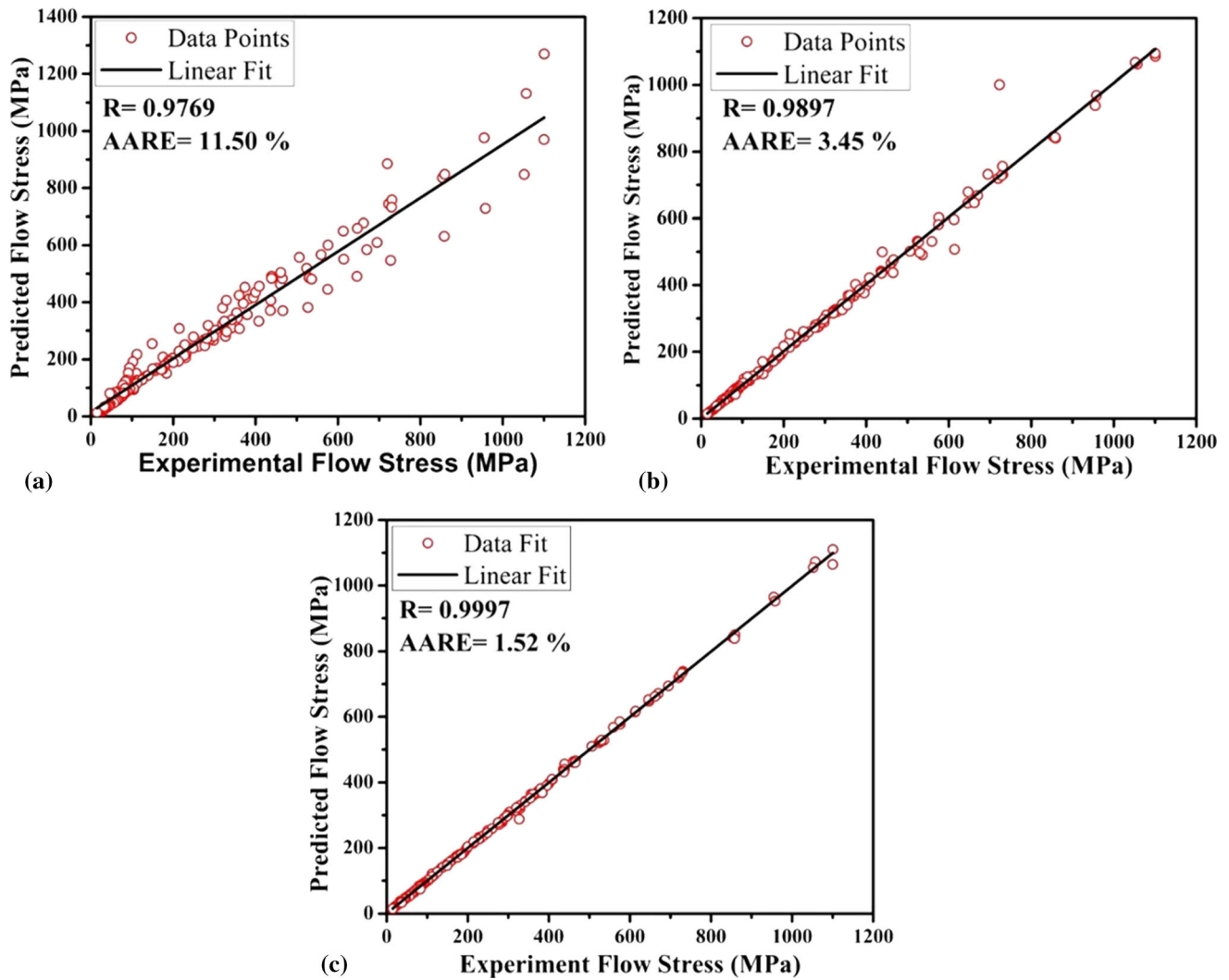Fig. 5 Mean square error during the training of the model (a) ANN model 1 and (b) ANN model 2

Fig. 6 Performance of models, (a) sine hyperbolic Arrhenius model (b) ANN model 1, and (c) ANN model 2

Figure 5(a) and (b) shows MSE convergence plot for ANN model 1 and model 2, respectively. Convergence to mean square error is 0.0027 saturated at epoch 29 for model 1, and 1.6062×10^{-4} is saturated at epoch 113 for model 2. The predictability of models is assessed by R and AARE. The R and AARE for models are formulated by equations (Ref 20):

$$R = \frac{\sum_{i=1}^{N} \left(\sigma_{ef}^i - \overline{\sigma_{ef}} \right) \times \left(\sigma_{pf}^i - \overline{\sigma_{pf}} \right)}{\sqrt{\sum_{i=1}^{N} \left(\sigma_{ef}^i - \overline{\sigma_{ef}} \right)^2 \times \sum_{i=1}^{N} \left(\sigma_{pf}^i - \overline{\sigma_{pf}} \right)^2}} \quad \text{(Eq 13)}$$

$$\text{AARE}(\%) = \frac{1}{N} \times \sum_{i=1}^{N} \left| \frac{\sigma_{ef}^i - \sigma_{pf}^i}{\sigma_{ef}^i} \right| \times 100 \quad \text{(Eq 14)}$$

where σ_{ef}^i and σ_{pf}^i are the experimental and predicted value of flow stress, respectively; $\overline{\sigma_{ef}}$ and $\overline{\sigma_{pf}}$ are the mean values of σ_{ef}^i and σ_{pf}^i, respectively. N is the total number of datasets used in the study. In the present study, results (R and AARE) obtained from different models are represented in Table 1. Figure 6(a)-(c) represents the variation between the targeted and predicted

flow stress for CoFeMnNiTi EHEA developed by the Arrhenius relation, ANN model 1, and ANN model 2, respectively.

3.4 Compressive Behavior of Co₂₅Fe₂₅Mn₅Ni₂₅Ti₂₀ EHEA

The true stress vs. strain plot is given in Fig. 3 (solid line represents the experimental flow curve for different thermomechanical processing parameters), which indicates the first stress value increases and reaches a peak value than a continuous reduction in stress values. The flow curve behavior is correlated to a mechanism of DRX or globularization of laves phase. It is mentioned in the author's previous work in HEA (Ref 16) that the initial microstructure contains α-phase (FCC), β-phase (BCC), and Ti₂ (Co, Ni) laves phase. The volume fraction of β-phase is very low compared to α-phase and laves phases. At the large strain, a saturation of flow curve occurs due to the DRX mechanism. In Fig. 3, experimental flow curve indicates a constant drop in stress values with further straining except at 0.001 and 0.01 s⁻¹ at 1273 K, indicating the globularization of laves phase during thermomechanical processing. The strength of materials can be improved by an interaction of dislocations or parent atoms/foreign phase particles, which can be obtained
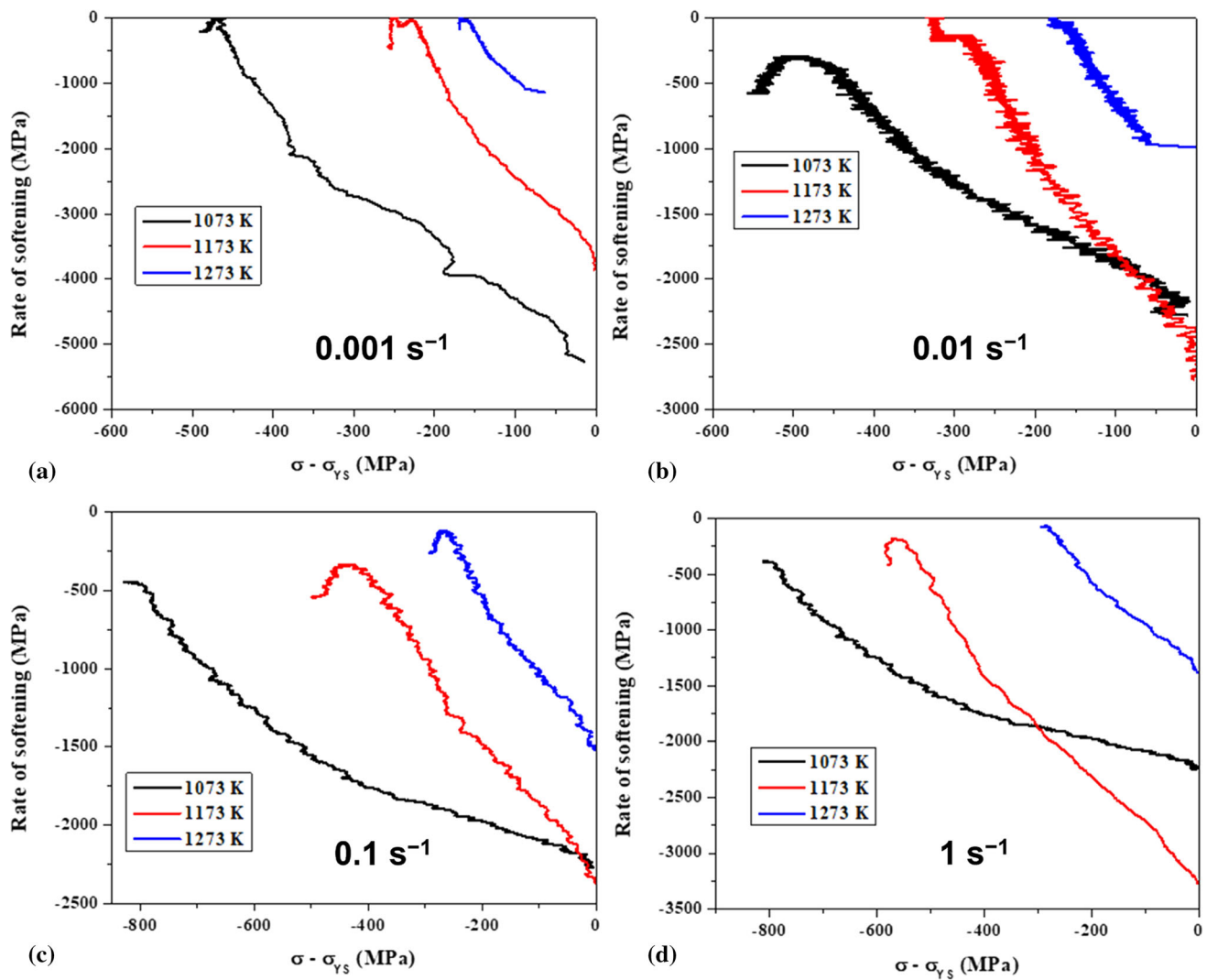
Fig. 7 Plot between rate of softening and stress

Table 2 Rate of softening values at different hot working conditions

Strain rate, s^{-1}	Temperature, K	θ_1	θ_2	θ_2/θ_1
0.001	1073	− 8.32	− 14.92	1.79
	1173	− 12.38	− 26.05	2.1
	1273	− 10.94	− 20.68	1.89
0.01	1073	− 2.67	− 5.65	2.11
	1173	− 6.31	− 9.37	1.48
	1273	− 5.2	− 8.15	1.56
0.1	1073	− 1.17	− 3.23	2.76
	1173	− 3.85	− 6.61	1.71
	1273	− 3.85	− 7.04	1.82
1	1073	− 1.14	− 3.7	3.24
	1173	− 4.2	− 8.51	2.02
	1273	− 3.49	− 5.99	1.71

by drawing the softening rate with stress values. The maximum stress value is subtracted to exclude the temperature effect on the microstructure and plotted in Fig. 7, which shows the softening rate with stress values. Each sample shows two softening values after the maximum stress. The values of softening rate are documented in Table 2.

It is noted that the initial softening rate is less compared to the softening rate values at a later stage. The softening rate depends on the grain's initial orientation with respect to the compression axis, resulting in the variation in softening rate either with rise in temperature at a fixed strain rate or with rise in strain rate at a fixed temperature. However, no regular trend in the values of softening rate is observed because of the variation in initial grain orientation with respect to the loading axis. The plot between mean free path and stress represents in Fig. 8, Bishoyi et al. (Ref 21) and Sahoo et al. (Ref 22) documented the details for the calculation of softening rate and mean free path. The mean free path of dislocation indicates a continuous increase in the value with strain which can be attributed to the breakdown of laves phases during deformation, which is attributed to cross slip of dislocations and the climb of dislocations. The climb and cross slip of dislocations increase the mean free path of dislocations with further deformation. The drop in the mean free path to zero value indicates that the
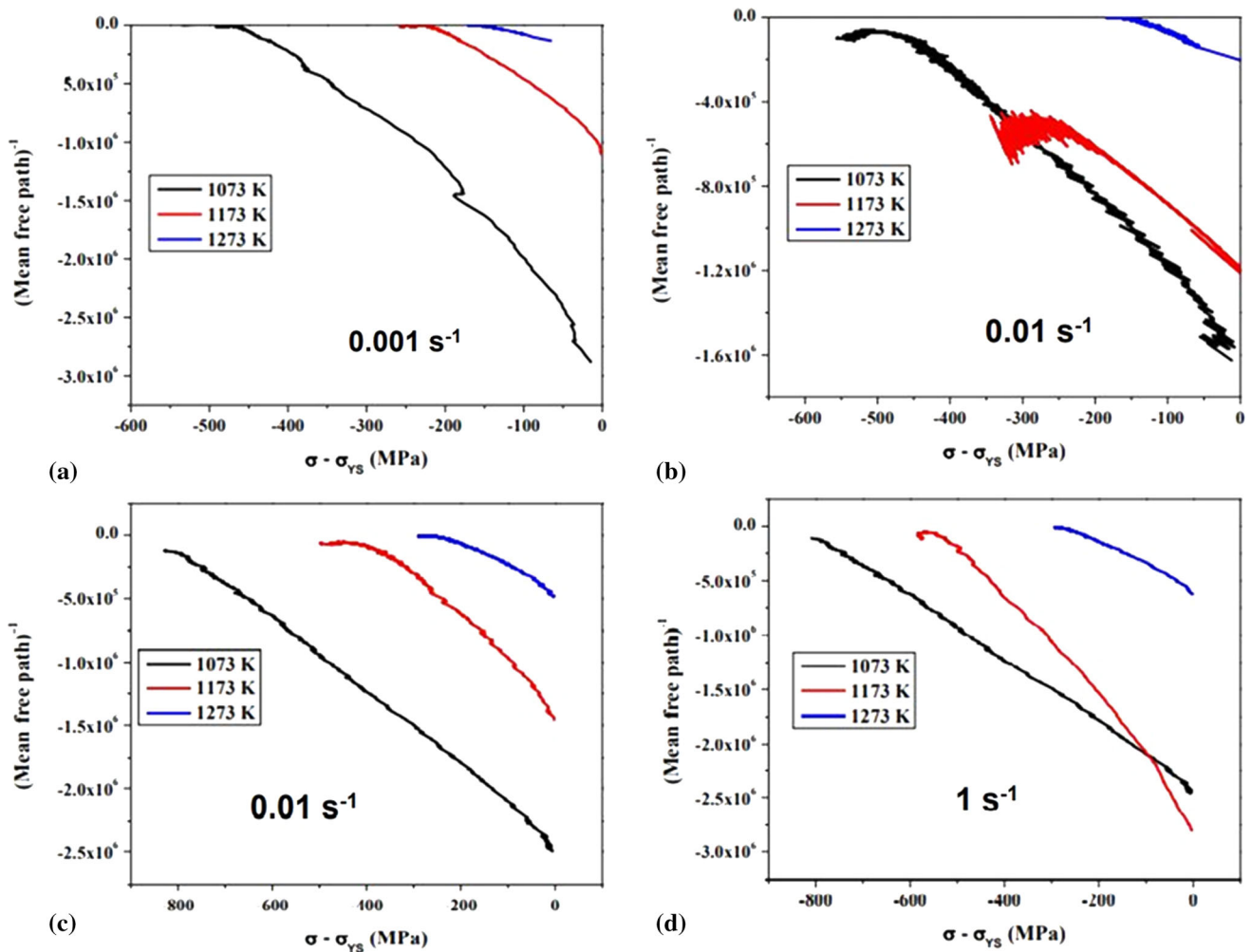
Fig. 8 Plot between mean free path and stress

completeness of globularization phenomenon during deformation, which is observed for the specimen deformed at 1273 K (strain rate range of 0.001-1 s^{-1}).

4. Microstructural Features of Deformed Sample

Microstructural characteristics of the hot deformed EHEA samples were carried out at different processing conditions of hot deformation. That study was considered for recognizing homogeneous and inhomogeneous deformation (pores, localized plastic flow, and adiabatic shear banding). The microstructural feature of deformed samples of EHEA deformed at different hot working conditions (1173 K and strain rate 1 s^{-1}, (b) 1173 K and strain rate 0.01 s^{-1}, (c) 1273 K and strain rate 1 s^{-1}) is represented in Fig. 9.

5. Mechanism of Microstructure Evolution

The starting microstructure contains the mixture of α-phase (white space present between the purple colors) and laves phase (purple color) as alternate lamellae in the grain (Fig. 10a). Reliance et al. (Ref 23) (Ref 6) reported the deformation

mechanism for single-phase $Co_{25}Cr_{20}Fe_{25}Ni_{25}V_5$ FCC high-entropy alloy and $(CoCrFeNi)_{90}Zr_{10}$ quasi-peritectic high-entropy alloy. The orientation of lamellae varies from one grain to next grain. Further, the microstructure contains the β-phase (see black color marks in Fig. 10a) randomly distributed in the grains. During deformation at high temperature, laves phase bends within the grains, and the extent of bending depends on the orientation of laves phase with respect to the loading axis. The bended laves phase of a grain (Fig. 10d) is shown in the magnified form in Fig. 10(e) where it is clearly observed that dislocations are piled up at the nose of the bend region. It is well known that atomic potential of laves phase is the maximum in the tip of the bend region and decreases towards its lateral sides. Since the deformation was done at high temperature, the high atomic potential of the tip of the bend region along with the enhanced pipe diffusion by the presence of dislocation breaks the single lamellae of laves phase into two lamellae (see Fig. 10f). This procedure is observed in the other grains of the microstructure during deformation. This breaking of laves phase lamellae facilitates the movement of dislocation further in the α-phase and enhances the dislocation–dislocation interaction. This breaking of laves phase at high temperature during deformation reflects in the drop of strength with an increase in the strain of the material. However, the breaking of the laves phase is incomplete in all the grains when deformation
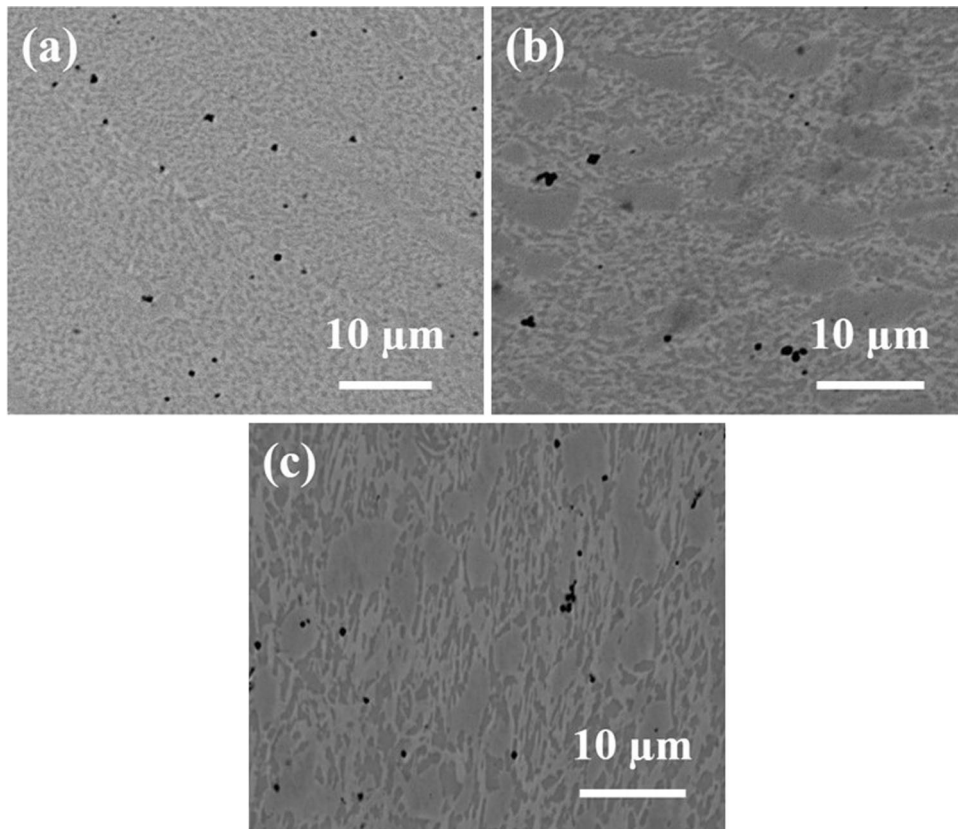
Fig. 9 SEM micrograph of deformed specimen (a) at temperature 1173 K and strain rate 1 s^{-1}, (b) at temperature 1173 K and strain rate 0.01 s^{-1}, (c) at temperature 1273 K and strain rate 1 s^{-1}

was carried out at a high strain rate or low temperature. The above observation is consistent with the microstructure obtained after deformation (see Fig. 9).

6. Conclusion

In Summary, the general framework is provided for predicting the flow curve during thermomechanical processing in EHEA using the empirical Arrhenius relation and the ANN models. It is noted that the ANN model with appropriate normalization of datasets can be utilized to predict the flow curve accurately at different ranges of temperatures and strain rates during the processing of materials as compared to the Arrhenius relation. Also, the proposed deformation mechanism indicates the breaking down of laves phase lamellae due to the pipe diffusion mechanism. Finally, the current study provides future opportunities to design new HEA materials using ANN approach for high-temperature applications.
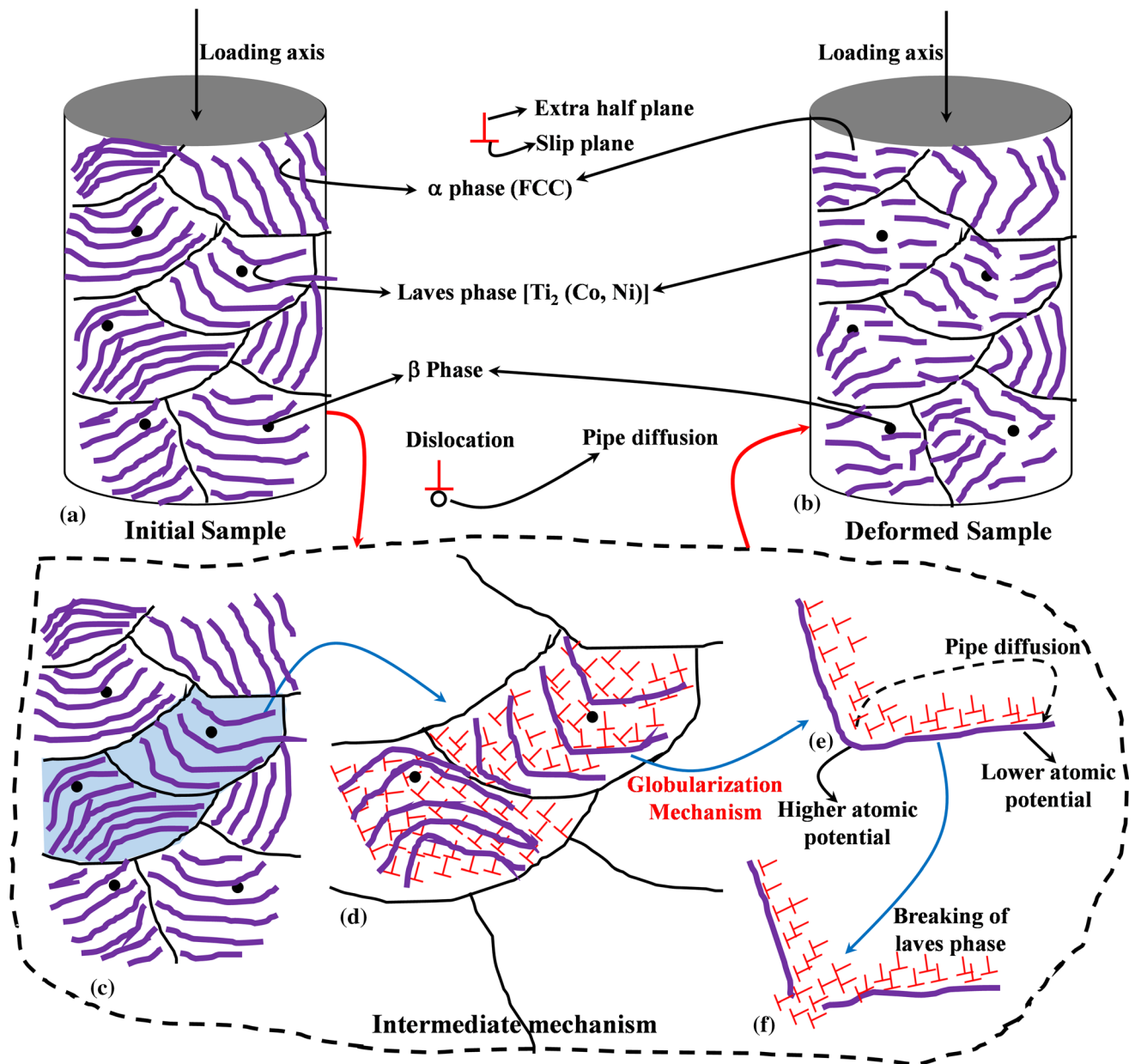
Fig. 10 Mechanism of eutectic HEA during deformation; (a) initial microstructure of alloy before deformation, (b) microstructure after deformation. The intermediate mechanism of microstructure evolution during deformation is shown in (c)-(f)

References

1. J.W. Yeh, S.K. Chen, S.J. Lin, J.Y. Gan, T.S. Chin, T.T. Shun, C.H. Tsau and S.Y. Chang, Nanostructured High-Entropy Alloys with Multiple Principal Elements: Novel Alloy Design Concepts and Outcomes, *Adv. Eng. Mater.*, 2004, **6**(5), p 299–303.

2. X. Jin, Y. Zhou, L. Zhang, X. Du and B. Li, A Novel Fe20Co20Ni41Al19 Eutectic High Entropy Alloy with Excellent Tensile Properties, *Mater. Lett.*, 2018, **216**(January), p 144–146.

3. W. Huo, H. Zhou, F. Fang, Z. Xie and J. Jiang, Microstructure and Mechanical Properties of CoCrFeNiZr x Eutectic High-Entropy Alloys, *Mater. Des.*, 2017, **134**, p 226–233. https://doi.org/10.1016/j.matdes.2017.08.030

4. K.K. Alaneme and E.A. Okotete, Recrystallization Mechanisms and Microstructure Development in Emerging Metallic Materials: A Review, *J. Sci. Adv. Mater. Devices*, 2019, **4**(1), p 19–33. https://doi.org/10.1016/j.jsamd.2018.12.007

5. N.D. Stepanov, D.G. Shaysultanov, N.Y. Yurchenko, S.V. Zherebtsov, A.N. Ladygin, G.A. Salishchev and M.A. Tikhonovsky, High Temperature Deformation Behavior and Dynamic Recrystallization in CoCrFeNiMn High Entropy Alloy, *Mater. Sci. Eng. A*, 2015, **636**, p 188–195. https://doi.org/10.1016/j.msea.2015.03.097

6. R. Jain, A. Jain, M.R. Rahul, A. Kumar, M. Dubey, R.K. Sabat, S. Samal and G. Phanikumar, Development of Ultrahigh Strength Novel Co-Cr-Fe-Ni-Zr Quasi-Peritectic High Entropy Alloy by an Integrated Approach Using Experiment and Simulation, *Materialia*, 2020, **14**, p 100896.

7. G.R. Johnson and W.H. Cook, Fracture Characteristics of Three Metals Subjected to Various Strains, Strain Rates, Temperatures and Pressures, *Eng. Fract. Mech.*, 1985, **21**(1), p 31–48.

8. F.J. Zerilli and R.W. Armstrong, Dislocation-Mechanics-Based Constitutive Relations for Material Dynamics Calculations, *J. Appl. Phys.*, 1987, **61**(5), p 1816–1825.

9. C.M. Sellars and W.J. McTegart, On the Mechanism of Hot Deformation, *Acta Metall.*, 1966, **14**(9), p 1136–1138.

10. Z.S. Motlagh, B. Tolaminejad and A. Momeni, Prediction of Hot Deformation Flow Curves of 1.4542 Stainless Steel, *Met. Mater. Int.*, 2020, **27**, p 2512–2529. https://doi.org/10.1007/s12540-020-00627-7

11. M. Patnamsetty, A. Saastamoinen, M.C. Somani and P. Peura, Constitutive Modelling of Hot Deformation Behaviour of a CoCr-FeMnNi High-Entropy Alloy, *Sci. Technol. Adv. Mater.*, 2020, **21**(1), p 43–55. https://doi.org/10.1080/14686996.2020.1714476

12. Z.L. Guoliang Ji, F. Li, Q. Li and H. Li, A Comparative Study on Arrhenius-Type Constitutive Model and Artificial Neural Network Model to Predict High-Temperature Deformation Behaviour in Aermet100 Steel, *Mater. Sci. Eng. A*, 2011, **528**(13–14), p 4774–4782. https://doi.org/10.1016/j.msea.2011.03.017

13. O. Sabokpa, A. Zarei-Hanzaki, H.R. Abedi and N. Haghdadi, Artificial Neural Network Modeling to Predict the High Temperature Flow Behavior of an AZ81 Magnesium Alloy, *Mater. Des*, 2012, **39**, p 390–396. https://doi.org/10.1016/j.matdes.2012.03.002

14. K. Singh, S.K. Rajput, T. Soota, V. Verma and D. Singh, Prediction of Hot Deformation Behavior of High Phosphorus Steel Using Artificial Neural Network, *IOP Conf. Ser. Mater. Sci. Eng.*, 2018, **330**(1), p 012038.

15. R. Jain, S.K. Dewangan, V. Kumar and S. Samal, Artificial Neural Network Approach for Microhardness Prediction of Eight Component FeCoNiCrMnVAlNb Eutectic High Entropy Alloys, *Mater. Sci. Eng. A*, 2020, **797**(August), p 140059. https://doi.org/10.1016/j.msea.2020.140059

16. R. Jain, M.R. Rahul, S. Samal, V. Kumar and G. Phanikumar, Hot Workability of Co-Fe-Mn-Ni-Ti Eutectic High Entropy Alloy, *J. Alloys Compd.*, 2020, **822**, p 153609.

17. J. Liu, H. Chang, T.Y. Hsu and X. Ruan, Prediction of the Flow Stress of High-Speed Steel During Hot Deformation Using a BP Artificial Neural Network, *J. Mater. Process. Technol.*, 2000, **103**(2), p 200–205.

18. J. Liu, X. Wang, J. Liu, Y. Liu, H. Li and C. Wang, Hot Deformation and Dynamic Recrystallization Behavior of Cu-3Ti-3Ni-0.5Si Alloy, *J. Alloys Compd.*, 2019, **782**, p 224–234. https://doi.org/10.1016/j.jallcom.2018.12.212

19. C. Zener and J.H. Hollomon, Effect of Strain Rate upon Plastic Flow of Steel, *J. Appl. Phys.*, 1944, **15**(1), p 22–32.

20. S. Srinivasulu and A. Jain, A Comparative Analysis of Training Methods for Artificial Neural Network Rainfall-Runoff Models, *Appl. Soft Comput. J.*, 2006, **6**(3), p 295–306.

21. B.D. Bishoyi, R.K. Sabat and S.K. Sahoo, Effect of Temperature on Microstructure and Texture Evolutions during Uniaxial Compression of Commercially Pure Titanium, *Mater. Sci. Eng. A Struct. Mater. Prop. Microstruct. Process.*, 2018, **718**, p 398–411. https://doi.org/10.1016/J.MSEA.2018.01.128

22. S.K. Sahoo, R.K. Sabat, B.D. Bishoyi, A.G.S. Anjani and S. Suwas, Effect of Strain-Paths on Mechanical Properties of Hot Rolled Commercially Pure Titanium, *Mater. Lett.*, 2016, **180**, p 166–169.

23. R. Jain, M.R. Rahul, P. Chakraborty, R.K. Sabat, S. Samal, G. Phanikumar and R. Tewari, Design and Deformation Characteristics of Single-Phase Co-Cr-Fe-Ni-V High Entropy Alloy, *J. Alloys Compd.*, 2021, **888**, p 161579.